Variable-Density Parallel Imaging With Partially Localized Coil Sensitivities

Tolga Çukur*, *Member, IEEE*, Juan M. Santos, *Member, IEEE*, John M. Pauly, *Member, IEEE*, and Dwight G. Nishimura, *Member, IEEE*

Abstract—**Partially parallel imaging with localized sensitivities is a fast parallel image reconstruction method for both Cartesian and non-Cartesian trajectories, but suffers from aliasing artifacts when there are deviations from the assumption of perfect localization. Such reconstructions would normally crop the individual coil images to remove the artifacts prior to combination. However, the sampling densities in variable-density k-space trajectories support different field-of-views for separate regions in k-space. In fact, the higher sampling density of low frequencies can be used to reconstruct a bigger field-of-view without introducing aliasing artifacts and the resulting image signal-to-noise ratio (SNR) can be improved. A novel, fast variable-density parallel imaging method is presented, which reconstructs different field-of-views from separate frequencies according to the local sampling density in k-space. Aliasing-suppressed images can be produced with high SNR-efficiency without the need for accurate estimation of coil sensitivities and complex or iterative computations.**

Index Terms—**Aliasing artifact, image reconstruction, parallel imaging, self calibration, variable density.**

I. INTRODUCTION

PARTIALLY parallel magnetic resonance imaging (MRI) methods utilize the spatial sensitivity of radio-frequency (RF) coils as an additional encoding mechanism to complement gradient encoding [1]–[9]. These techniques can improve the robustness of many MRI methods by reducing the number of data samples and the acquisition times as well as the load on the gradient hardware. Since the gradient performance is limited more by physiological factors than hardware issues, parallel imaging opens the door to new applications that are not viable with conventional gradient encoding. Nevertheless, the success of all parallel imaging techniques inherently depends on the reliability of the reconstruction algorithm that recovers the missing data.

Image reconstruction methods for parallel imaging can be grouped into three main categories: k-space, image-domain, and hybrid methods. The missing samples are computed in k-space for methods such as the simultaneous acquisition of spatial harmonics (SMASH) [4] and generalized autocalibrating partially parallel acquisition (GRAPPA) [5]. On the other hand, the sensitivity encoding (SENSE) [6] and partially parallel imaging with localized sensitivities (PILS) [7] methods work in the image domain. There are also hybrid techniques such as sensitivity profiles from an array of coils for encoding and reconstruction in parallel (SPACE RIP) [8].

An important step of the reconstruction is an accurate estimation of the coil sensitivities for some of the aforementioned methods. SMASH and SENSE are effective techniques; however, undesirable imaging conditions such as patient or coil motion will compromise the accuracy of the sensitivity estimation and reduce the image quality. In contrast, autocalibrating approaches yield more reliable profile estimates by collecting additional data in the central k-space region [5], [10]–[14]. These methods employ variable-density k-space trajectories, which can increase imaging speed or resolution by undersampling the high-spatial-frequency components [15].

Parallel imaging techniques have been tailored to handle variable-density non-Cartesian acquisitions [5], [8], [16]–[19]; however, most k-space and image-domain methods require iterations of high computational complexity to render good quality reconstructions. This computational burden hinders the applicability of these methods to non-Cartesian trajectories. While several modifications have been recently proposed for reducing processing times [20]–[25], the PILS method can readily perform very fast reconstructions for variable-density non-Cartesian acquisitions [26]–[28].

PILS allows direct reconstruction of individual coil images for arbitrary k-space trajectories and does not require accurate sensitivity estimates. The acquisition speed is increased by performing Nyquist sampling for only a fraction of the entire field-of-view (FOV), namely the local imaging FOV associated with a particular coil. The localized sensitivity of each coil suppresses the severe aliasing artifacts due to undersampling. However, the artifact suppression is compromised when this assumption of coil localization does not hold, i.e., the spatial extent of the coil sensitivity allows signal reception from outside the prescribed local imaging FOV.

In practice, the orientations and sensitivities of many coil arrays do not fulfill the condition of perfect localization. Therefore, significant aliasing artifacts might remain in the sum-of-squares combination of the individual coil images. A simple solution is to remove the pixels with artifacts from the individual images; however, this approach does not make efficient use of

*T. Çukur is with the Information Systems Laboratory, Department of Electrical Engineering, Stanford University, Stanford, CA 94305 USA (e-mail: cukur@stanford.edu).

J. M. Santos, J. M. Pauly, and D. G. Nishimura are with the Information Systems Laboratory, Department of Electrical Engineering, Stanford University, Stanford, CA 94305 USA.
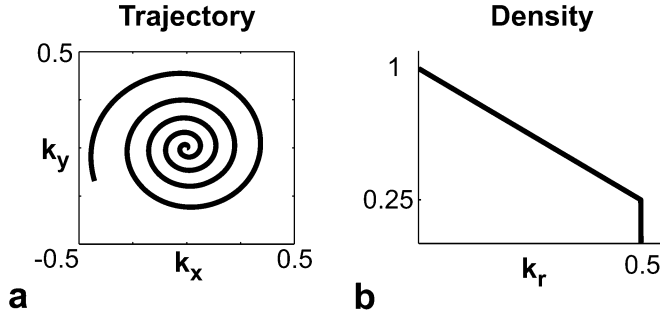
Fig. 1. a: An interleaf of a variable-density spiral trajectory with normalized k-space coordinates. b: The corresponding sampling density as a function of k-space radius. The relative density falls off to one-fourth at the periphery of k-space.
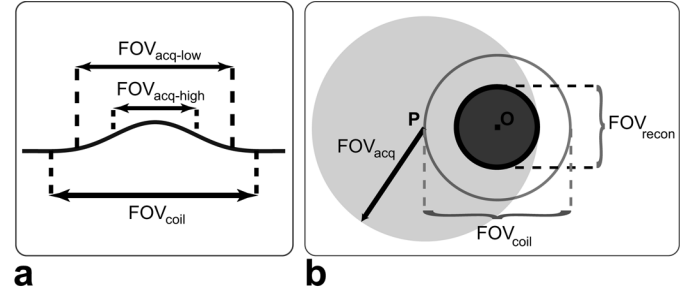

Fig. 2. a: The spatial extent of the coil sensitivity ($\mathrm{FOV_{coil}}$) is shown along with $\mathrm{FOV_{acq}}$ for low and high spatial frequencies. b: The worst-case for aliasing artifacts arises from an object located at the edge of $\mathrm{FOV_{coil}}$ (point P). To completely suppress the resulting artifacts within $\mathrm{FOV_{recon}}$ (centered at point O), the condition expressed in (1) must be met.

the data and reduces the SNR. Alternatively, artifact-free reconstructions can be maintained within the spatial sensitivity extent of the array elements, while the SNR is improved by effectively utilizing the oversampled central k-space data in variable-density acquisitions.

We propose a new variable-density parallel imaging method that reconstructs images with reduced artifacts and high SNR-efficiency, without the need for accurate estimation of the coil sensitivities. This method combines the individual coil images in a single step without complex or iterative computations. As a result, fast and artifact-suppressed parallel image reconstructions can be provided for both non-Cartesian and Cartesian variable-density trajectories, easing the clinical utilization of parallel MRI.

II. METHODS

For variable-density k-space trajectories, the sampling densities at low- and high-spatial-frequencies support different acquisition FOVs ($\mathrm{FOV_{acq}}$). Fig. 1 displays an interleaf of a variable-density spiral trajectory and the corresponding variation in density as a function of k-space radius. A higher sampling density is observed around the k-space origin compared to the periphery. Therefore, low-spatial-frequency components are oversampled when the sampling density for high-frequency-components matches the Nyquist rate within the local imaging FOV. When the reconstruction FOV ($\mathrm{FOV_{recon}}$) is tailored according to the highest sampling density, aliasing artifacts are introduced. To avoid these artifacts, PILS normally chooses the $\mathrm{FOV_{recon}}$ supported by the lowest density. In that case, however, more-densely-sampled low-spatial-frequency data are ineffectively utilized.

Alternatively, the lower-frequency samples can be used to reconstruct a larger FOV without introducing any aliasing artifacts. Fig. 2(a) shows the sensitivity of an array element in relation to the $\mathrm{FOV_{acq}}$s for low and high frequencies. Aliasing artifacts can be avoided by determining $\mathrm{FOV_{recon}}$ separately for these two sets of frequencies. Given $\mathrm{FOV_{acq}}$ and the spatial extent of the coil sensitivity ($\mathrm{FOV_{coil}}$), $\mathrm{FOV_{recon}}$ should ideally satisfy the following condition:

$$\mathrm{FOV_{recon}} = \begin{cases} \mathrm{FOV_{acq}}, & \text{if } \mathrm{FOV_{coil}} \leq \mathrm{FOV_{acq}} \\ 2\mathrm{FOV_{acq}} - \mathrm{FOV_{coil}}, & \\ & \text{if } \frac{\mathrm{FOV_{coil}}}{2} \leq \mathrm{FOV_{acq}} < \mathrm{FOV_{coil}} \\ 0, & \text{otherwise.} \end{cases} \quad (1)$$

High-spatial-frequency components:

Low-spatial-frequency components:
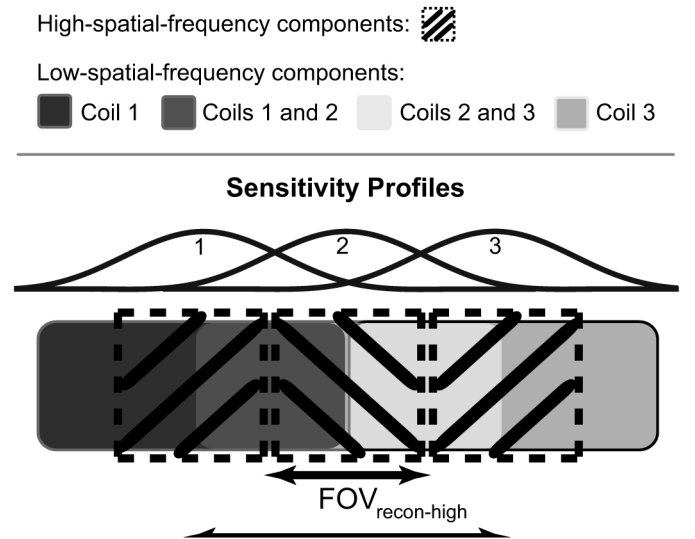
 Coil 1 Coils 1 and 2 Coils 2 and 3 Coil 3

Fig. 3. $\mathrm{FOV_{recon}}$s supported by low- and high-spatial-frequency data are displayed for individual coils in a 1-D array. While the Nyquist-sampled region for high frequencies ($\mathrm{FOV_{recon-high}}$) is relatively limited, oversampled low-frequency data can be reconstructed in a larger spatial extent $\mathrm{FOV_{recon-low}}$. As a result, overlapping regions of low-frequency component images are generated between adjacent coils, marked with different colors.

The above relations ensure complete removal of aliasing artifacts by considering the worst-case scenario, i.e., an object placed on the periphery of $\mathrm{FOV_{coil}}$ as shown in Fig. 2(b). However, this condition is overly stringent in most cases, and can lead to suboptimal utilization of collected data. First of all, the coil sensitivity is substantially lower towards the edge of $\mathrm{FOV_{coil}}$. This dampens the image intensities of both the object and the resulting artifacts. Furthermore, undersampling is mostly performed for higher frequencies in variable-density acquisitions, which creates well-behaved artifacts that appear as random noise and reduce the image SNR [15]. Finally, the expressed conditions for $\mathrm{FOV_{acq}} < \mathrm{FOV_{coil}}$ can significantly limit spatial resolution. Therefore, in this work, we adopted a weaker constraint, $\mathrm{FOV_{recon}} = \mathrm{FOV_{acq}}$, to maintain a more favorable trade-off between resolution and SNR.

Example $\mathrm{FOV_{recon}}$s pertaining to low- and high-spatial-frequency components are displayed in Fig. 3 for a sample 1-D coil array. The higher sampling densities at lower frequencies will cause $\mathrm{FOV_{recon}}$ to be larger than nominal. As a result, the

low-frequency data will be averaged over a larger spatial extent among array elements, improving the image SNR.

In the following sections, we will first describe a method for variable-FOV reconstruction of single-coil data, followed by a simple and efficient voxel-wise combination of the individual coil images. Afterward, the noise characteristics of the resulting image will be analyzed. Finally, we will outline the *in vivo* experiments designed to demonstrate the reliability of the proposed technique.

A. Individual Coil Images

The local distance between neighboring k-space points determines the spatial region in which a certain frequency component is Nyquist sampled, namely $\mathrm{FOV_{acq}}$. As a result, this component will lead to aliasing artifacts when used to reconstruct an FOV larger than that supported by the local sampling density. On the other hand, if $\mathrm{FOV_{recon}}$ is limited to $\mathrm{FOV_{acq}}$, the aliasing-artifact and noise contribution of the component can be substantially reduced.

A variable-FOV reconstruction is a spatially-variant system by nature, which cannot be implemented with a single convolution operation in the image domain. In contrast, if the data are partitioned into distinct regions of space (in the image domain) or frequency (in k-space), then each partition can be treated with a spatially-invariant system. While we would ideally like to vary $\mathrm{FOV_{recon}}$ continually, the computational complexity scales with the number of partitions. Assuming this number is gradually increased, the initial steps yield the highest levels of improvement in artifact suppression [29]. In practice, efficient and high-quality reconstructions can be maintained using a limited degree of discretization.

In previous work, the extent of the gridding kernel was varied over k-space to implement the aforementioned reconstruction [29]. Although this strategy offered an intuitive link between the kernel extent and the distance between k-space samples, we adopted an image-domain approach to reduce the computational load for parallel imaging. The proposed algorithm starts with a conventional gridding reconstruction

$$m_o(r) = \frac{1}{c(r)} \left\{ [c(r)m_s(r)] * \mathrm{I\!I\!I}\left(\frac{r}{\alpha \mathrm{FOV_{max}}}\right) \right\} \quad (2)$$

where r is the spatial coordinate, $m_o(r)$ is the reconstructed image, $m_s(r)$ is the Fourier transform of the density-compensated k-space data, and $c(r)$ is the Fourier transform of the gridding kernel $C(k)$. The Shah sampling function is denoted with $\mathrm{I\!I\!I}(r)$, where α is the oversampling factor and $\mathrm{FOV_{max}}$ is $\mathrm{FOV_{acq}}$ supported by the highest sampling density.

Afterward, the data are partitioned into slabs in k-space for Cartesian trajectories, and annuli for spiral and radial trajectories as shown in Fig. 4. For each partition, the mean distance between adjacent k-space samples can be used to determine $\mathrm{FOV_{acq}}$, and the elements in each partition can then be used to reconstruct the corresponding $\mathrm{FOV_{recon}}$. The effective output can be expressed as

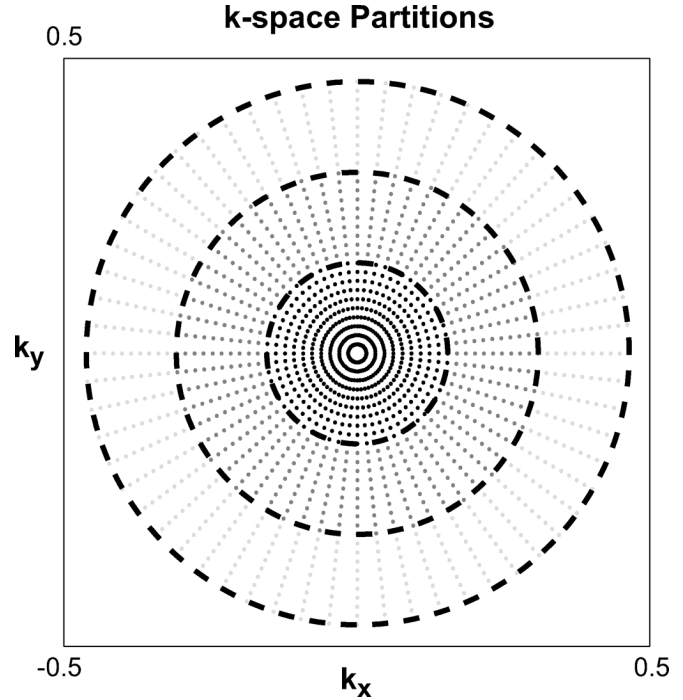$$m_v(r) = \sum_{i=1}^{N} a_i(r) \left[b_i(r) * m_o(r) \right] \quad (3)$$

Fig. 4. An example partitioning of k-space samples into several annuli. Each partition is reconstructed within $\mathrm{FOV_{recon}}$ supported by the corresponding mean sampling density.

where $b_i(r)$ is an ideal band-pass filter that suppresses all spatial frequencies except those in the corresponding k-space partition Z_i, and $a_i(r)$ is an ideal apodization function that only supports $\mathrm{FOV^i_{recon}}$ assigned to Z_i. The resultant image $m_v(r)$ has a full-resolution central region, and the resolution gradually decreases toward the edges of the image. Fig. 5 demonstrates an example where the object is a superposition of two sinusoids and k-space is partitioned into two subsets, namely the low- and high-spatial-frequency components.

Although $m_v(r)$ for a given coil has reduced peripheral resolution, the remaining array elements can provide the missing high-frequency data at those spatial locations. The final combined image will then not suffer from any resolution loss. On the other hand, if high spatial frequencies are very heavily undersampled, the combined $\mathrm{FOV_{recon}}$ of all coils may not cover the entire region-of-interest (ROI). In such cases, the minimum $\mathrm{FOV_{recon}}$ should be limited to avoid blurring and maintain complete coverage, at the possible expense of additional noise-like aliasing from high-frequency data.

B. Combination of Coil Images

Once the individual coil images are reconstructed with the variable-FOV method, we perform an optimal linear combination to assemble the entire image FOV. Nevertheless, the combination weights should be carefully tailored to yield high-quality reconstructions. When sample noise data are collected, noise decorrelation can be performed as a first step to generate a new set of coil sensitivities and k-space data through a linear mapping [16]. Although this helps minimize the image noise, the resulting SNR improvements reported in literature are relatively small, e.g., an approximate maximum of 7% [30], even with
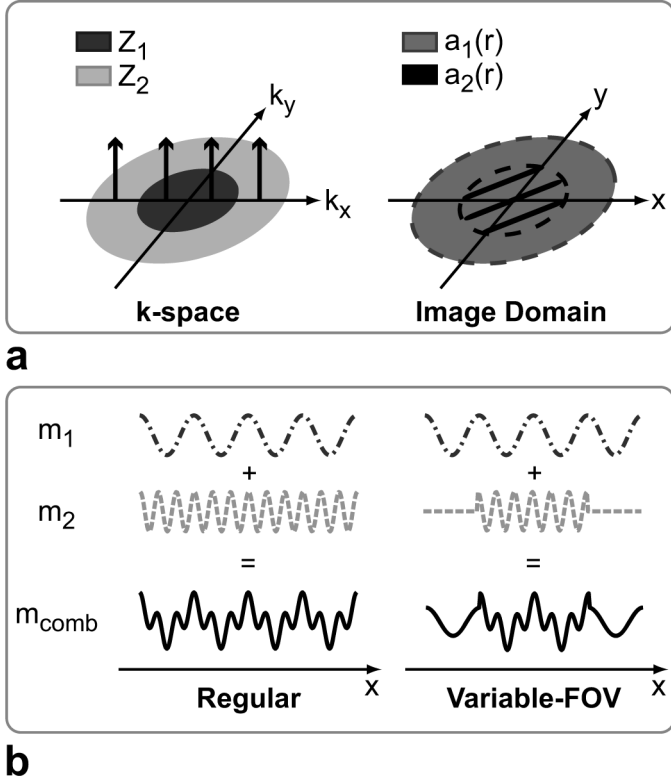
a

b

Fig. 5. a: Example k-space partitions (Z_i) and apodization functions ($a_i(r)$) for the variable-FOV reconstruction of an object, which is the superposition of two sinusoids varying in the x-direction. The impulses within the inner partition Z_1 represent the low-frequency sinusoid (m_1), while the high-frequency components (m_2) fall into the outer subset Z_2. In the image domain, $a_{1,2}(r)$ are represented with circular disks bounded by the outer and inner dashed circles, respectively. While $a_1(r)$ for low spatial frequencies is relatively broader, $a_2(r)$ applies a tighter apodization to reduce $\text{FOV}_{\text{recon}}$ for high frequencies. b: Cross-sections from regular and variable-FOV reconstructions of the component images ($m_{1,2}$) are shown along with the combination (m_{comb}). For the variable-FOV image, m_1 is maintained within the entire FOV while the spatial extent of m_2 is limited by that of $a_2(r)$. Therefore, the central part of the image has full resolution, whereas only the low-frequency components are retained in the outer part.

considerable levels of correlation among the array elements. Furthermore, the obtained estimates may not be accurate enough to sufficiently reduce these correlation levels [31]. In such cases, the decorrelation step can be omitted to reduce the computational load and avoid potential reconstruction errors.

To maximize SNR, the weight for each coil should equal the complex conjugate of its sensitivity normalized by the sum-of-squares (SOS) combination of all sensitivities [32]. The sensitivity for a given coil is estimated by first obtaining a lower-resolution image from oversampled central k-space data, extracted through Fourier domain truncation. Afterward, the sensitivity profile is computed as the ratio of this image to the SOS combination of such images from all coils [32].

It is also essential to determine the weights separately for low- and high-spatial-frequency component images. Extending $\text{FOV}_{\text{recon}}$ increases the probability of overlap between different array elements (Fig. 3). Hence, at a given pixel, more coils contribute to low-frequency data than that for high frequencies, resulting in an overweighting of low frequencies accompanied

by image blurring. To restore the balance among different subsets of frequencies, the weighted average for each subset should be separately computed among the coils with signal contribution. Although the analysis can be easily generalized, we will assume only two subsets for simplicity. The resultant image (P) can then be expressed as a linear combination of the low- and high-frequency images (S_i^L and S_i^H) reconstructed with the variable-FOV method

$$P = \sum_i \left(S_i^L w_i^L + S_i^H w_i^H \right) \tag{4}$$

where S_i^L and S_i^H are null outside the corresponding $\text{FOV}_{\text{recon}}$. The combination weights w_i^L, w_i^H for the low- and high-frequency images are

$$w_i^L = \frac{I_i^L D_i^*}{\sqrt{\sum_k I_k^L |D_k|^2}} \tag{5}$$

$$w_i^H = \frac{I_i^H D_i^*}{\sqrt{\sum_k I_k^H |D_k|^2}}. \tag{6}$$

Here, D_i is the low-resolution image from the ith coil reconstructed after Fourier domain truncation. The indicator functions $I_i^{L,H}$ determine which set of coils will be used for computing the weights at each pixel

$$I_i^{L,H} = \begin{cases} 1, & \text{if } S_i^{L,H} \neq 0 \\ 0, & \text{otherwise.} \end{cases} \tag{7}$$

In other words, the indicator functions are set to zero for pixels outside the corresponding $\text{FOV}_{\text{recon}}$.

C. SNR Analysis

To characterize the image SNR, we can first derive the autocorrelation function of the image and determine the noise variance with respect to spatial location. If P is the image intensity at location (x, y) and $\tilde{P}^*$ is the conjugate intensity at $(\tilde{x}, \tilde{y})$, the autocorrelation can be expressed as

$$R_P = \text{E}\left\{ P(x,y)P^*(\tilde{x}, \tilde{y}) \right\}. \tag{8}$$

Following a series of reasonable assumptions, this function can be simplified and the variance of P at a given pixel can be computed as shown in the Appendix

$$\sigma_P^2 = A^L \sum_{i,j} \sigma_{ij}^2 W_{ij}^L(x,y) + A^H \sum_{i,j} \sigma_{ij}^2 W_{ij}^H(x,y). \tag{9}$$

Here, $W_{ij}^{L,H} = w_i^{L,H}(w_j^{L,H})^*$, and $A^{L,H}$ are constants proportional to the net area under the filters $B^{L,H}$ as expressed in (20) and (21). For the case of *a priori* noise decorrelation, the variance follows the relation $\sigma_P^2 = \sigma^2$ derived in (23), where σ^2 is the variance of the underlying Gaussian noise process. Note that the proposed reconstruction produces colored noise when I_i^L and I_i^H are not equal.

Meanwhile, the signal can be expressed as the expected value of the image (P)

$$\mu_P = \sum_i \text{E}\left\{ S_i^L w_i^L + S_i^H w_i^H \right\}. \tag{10}$$

The low- and high-spatial-frequency component images are the sensitivity-weighted versions of the imaged object, $M(x, y)$, namely $S_i^L = M^L D_i^L$ and $S_i^H = M^H D_i^H$. Using these expressions in (10)

$$\mu_P = \sum_i \left(\mathrm{E}\{M^L\} D_i^L w_i^L + \mathrm{E}\{M^H\} D_i^H w_i^H \right)$$

$$= \mathrm{E}\{M^L\} \sqrt{\sum_i I_i^L |D_i|^2} + \mathrm{E}\{M^H\} \sqrt{\sum_i I_i^H |D_i|^2}. \tag{11}$$

Finally, the SNR of the reconstruction can be computed as

$$\mathrm{SNR} = \frac{1}{\sigma_P^2} \left(\mathrm{E}\{M^L\} \sqrt{\sum_i I_i^L |D_i|^2} \right.$$

$$\left. + \mathrm{E}\{M^H\} \sqrt{\sum_i I_i^H |D_i|^2} \right). \tag{12}$$

Because $\mathrm{FOV}_{\mathrm{recon}}$ is larger for low frequencies, the proposed reconstruction broadens the spatial extent over which I_i^L is unity. As a result, the image SNR is enhanced through increased averaging of low-spatial-frequency data compared with regular PILS.

D. Experiments

For *in vivo* demonstrations, coronary angiography was performed in a single breath-hold with cardiac-gated gradient-echo sequences and spiral k-space trajectories [33]. The data were collected using a custom real-time system [34] and an 8-channel cardiac array, on a 1.5 T GE Signa Excite scanner with CV/i gradients (40 mT/m maximum strength and 150 T/m/s maximum slew rate). Following interactive real-time localization, the subjects were asked to hold their breath. When necessary, final adjustments to the imaging FOV were accomplished immediately prior to data acquisition. The common set of parameters for all experiments were a 4.5-mm slice thickness and spectral-spatial fat saturation [35].

For the proposed reconstruction, the data were first density-compensated using Voronoi-diagram-based estimates of the sampling density [36], [37]. The gridding reconstructions were then performed on a 512×512 grid with a three-pixel-wide Kaiser-Bessel kernel and an oversampling factor of 2 [38]. The noise correlation was estimated from signal-free background regions of these initial images by averaging over approximately 1000 pixels. The coils were found to be weakly correlated, and the decorrelation step yielded a maximum SNR gain of 3.5% in all datasets. Because the overall improvement was rather small, this additional step was omitted for simplicity and efficiency.

Afterward, $\mathrm{FOV}_{\mathrm{recon}}$ was determined as a function of k-space radius using the distance between adjacent samples. For computational efficiency, the data were partitioned according to $\mathrm{FOV}_{\mathrm{recon}}$, and a discretization step size of 4 cm was found sufficient for obtaining high-quality reconstructions. Smaller step sizes did not yield noticeable differences in artifact suppression or image resolution. Considering an ROI diameter of approximately 34 cm for the chest, the minimum $\mathrm{FOV}_{\mathrm{recon}}$ was limited to 17 cm. For $\mathrm{FOV}_{\mathrm{recon}}$ values below this limit, the corresponding partitions were combined.

The k-space data in each partition were then transformed into the image domain. To avoid abrupt variations in signal intensity, the apodization functions ($a(r)$) were chosen as Fermi windows with a full-width at half-maximum (FWHM) equal to the corresponding $\mathrm{FOV}_{\mathrm{recon}}$ and a transition width of 6 pixels. Meanwhile, the coil sensitivities were estimated from the central k-space samples within a diameter of 0.06, assuming a normalized maximum of 1. Finally, separate sets of spatial-frequency component images were combined using the weights calculated from the estimated sensitivities.

All data were processed using custom-written MATLAB code (Version 7, The MathWorks, Natick, MA) on a personal computer (PC) with a 2 GHz AMD CPU.

1) Comparison With SENSE: To demonstrate the differences between the proposed reconstruction and SENSE, one set of uniform- and three sets of variable-density spiral data were collected with 1-mm in-plane resolution. The following sets of parameters were prescribed for these acquisitions: acceleration factors $(R) = (1.1, 2.3, 3.4, 4.5)$, $(19, 13, 9, 7)$ interleaves, and $(15, 11, 11, 11)$-ms readouts. $\mathrm{FOV}_{\mathrm{acq}}$ was designed to be 30 cm for the uniform-density trajectory, whereas it linearly decreased from 30 to $(16, 8, 4)$ for the three variable-density spirals, respectively. Even for the uniform-density acquisition, the central part of the spiral trajectory was inherently oversampled due to gradient limitations. While the uniform-density data were reconstructed with $\mathrm{FOV}_{\mathrm{recon}} = 34, 30$ cm in two partitions, the remaining acquisitions were partitioned into five sets with $\mathrm{FOV}_{\mathrm{recon}} = 34, 30, 26, 22, 18$ cm.

The datasets were also reconstructed with SENSE, using an iterative conjugate-gradient solution as detailed in [16]. Because the overall SNR improvement due to noise decorrelation was limited to 3.5%, this step was again omitted. To enhance the accuracy of the aforementioned sensitivity estimates, a restricted ROI was manually selected to only contain the imaged object, and the estimates in this region were further processed with fourth-order polynomial fitting. For all acceleration factors, a total of approximately 10–14 iterations was observed to yield a sufficient level of artifact suppression. Therefore, the reconstruction was manually stopped to avoid further noise amplification.

2) Comparison With PILS: To compare the performance of the proposed method with PILS, uniform- and variable-density spiral data were collected with 0.8-mm in-plane resolution. The following parameters were prescribed for the uniform-density trajectory: a 20-cm FOV, $R = 1.7$, 18 interleaves, and 16-ms readouts. The data were partitioned into three sets, which were reconstructed with $\mathrm{FOV}_{\mathrm{recon}} = 28, 24, 20$ cm. For the variable-density acquisition, on the other hand, the parameters were an FOV linearly decreasing from 20 to 8 cm, $R = 4.5$, 18 interleaves, and 6-ms readouts. In this case, three partitions were used with $\mathrm{FOV}_{\mathrm{recon}} = 24, 20, 17$ cm.

Separate PILS reconstructions of the same data were also computed assuming either the largest or the smallest $\mathrm{FOV}_{\mathrm{recon}}$ among all partitions. While the former was used to display the
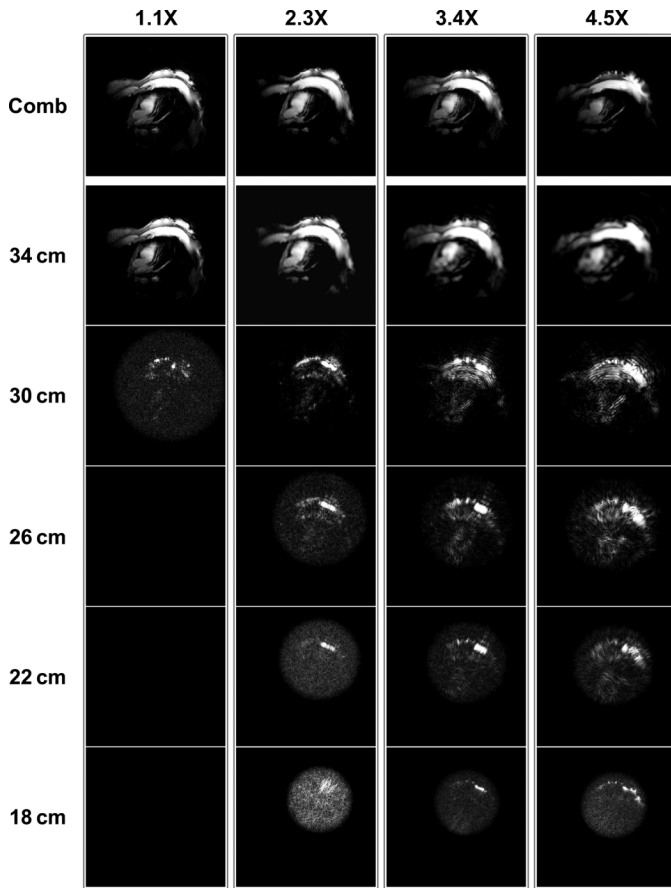
Fig. 6. The variable-FOV reconstructions of data from a single coil at various acceleration factors, $R = 1.1, 2.3, 3.4, 4.5$. While the top row represents the combined image for each factor, the remaining rows display the component images of different k-space partitions reconstructed with $\mathrm{FOV}_{\mathrm{recon}} = 34, 30, 26, 22, 18$ cm. The combined images have a central full-resolution region of size equal to the minimum $\mathrm{FOV}_{\mathrm{recon}}$. For higher R, the increased fall-off rate in sampling density lowers the amount of high-frequency samples contained in all partitions (except for the outermost). This shrinks the central k-space partition, reducing the resolution of the corresponding image ($\mathrm{FOV}_{\mathrm{recon}} = 34$ cm). Similarly, the structure of the object becomes more visible in smaller-FOV images due to increased low-frequency content.
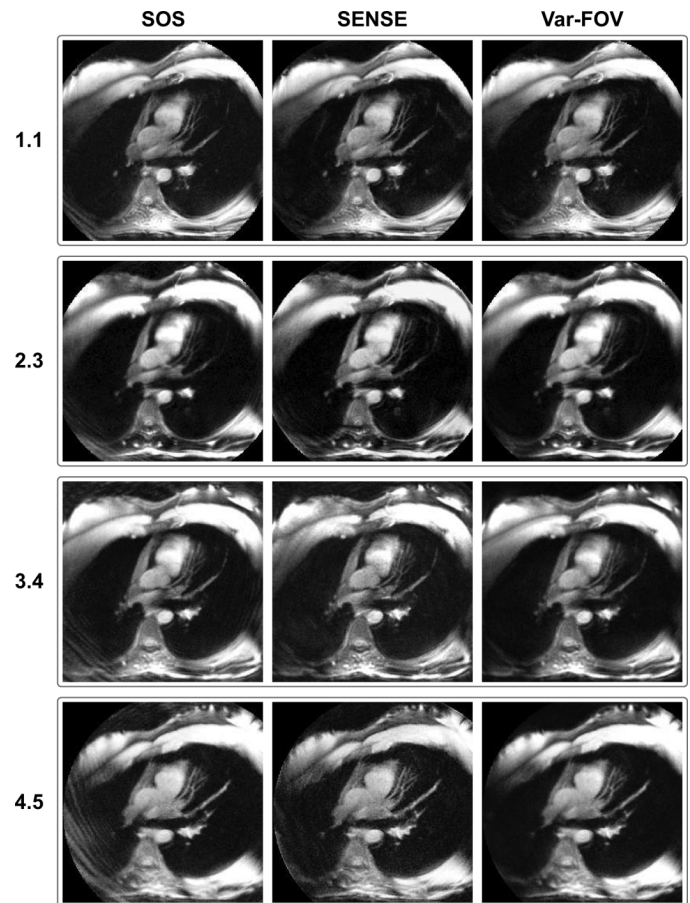

Fig. 7. Sum-of-squares (SOS), SENSE, and variable-FOV reconstructions of coronary angiograms collected at various acceleration factors, $R = 1.1, 2.3, 3.4, 4.5$. While severe aliasing artifacts are observed in the SOS images, both the SENSE and variable-FOV images demonstrate effective artifact suppression. At higher accelerations, SENSE suffers increasingly from the poor conditioning of the encoding matrix (equivalently, increased g-factor).

differences between the two techniques in terms of artifact suppression, the latter was used in comparative SNR measurements. These measurements were performed in identical locations of the reconstructed images. A total of five regions containing homogeneous blood or muscle signal were selected in the vicinity of the coronary vessels. To minimize measurement errors due to the spatially-variant nature of noise, the standard deviation of noise was also estimated within the corresponding signal regions. A minimum of 150 pixels were contained in each region.

III. RESULTS

To demonstrate the algorithm of the proposed method, component images reconstructed from separate k-space partitions are displayed in Fig. 6 along with the combined image for a single coil and acceleration factors of $R = 1.1, 2.3, 3.4, 4.5$. For higher accelerations, the frequencies of samples in each partition are lowered, including the central segment but excluding the outermost. Although this reduces the resolution of the component images reconstructed from the inner segments,

the aliasing artifacts are suppressed. Furthermore, the final image does not suffer from any resolution loss, as long as the remaining coils provide the missing high-frequency data at the edge of $\mathrm{FOV}_{\mathrm{recon}}$.

Fig. 7 shows the SOS, SENSE, and variable-FOV reconstructions of the aforementioned data collected with $R = 1.1, 2.3, 3.4, 4.5$. Although the SOS images have severe aliasing, both SENSE and the variable-FOV method effectively suppress these artifacts. Meanwhile, SENSE suffers from g-factor-related noise amplification at higher accelerations due to poor conditioning of the encoding matrix [6]. It is important to note that the variable-FOV method provides much shorter reconstruction times than the iterative SENSE method, as expected. Table I lists the reconstruction times at each acceleration factor, demonstrating up to an order of magnitude improvement with the proposed technique.

Fig. 8 validates the improved artifact-suppression capability of the variable-FOV method compared with PILS at two acceleration factors, $R = 1.7, 4.5$. While the PILS images suffer from residual aliasing artifacts, the variable-FOV method reliably suppresses both the more structured and the noise-like aliasing from low and high frequencies, respectively. Furthermore, this method achieves improved SNR compared with a

Acceleration	Samples	**SENSE**	**Variable-FOV**
R = 1.1	72257	334 s	33 s
R = 2.3	36036	163 s	28 s
R = 3.4	23967	133 s	26 s
R = 4.5	19474	121 s	24 s

For each acceleration factor, the number of k-space samples per coil is listed along with the total reconstruction times for data from 8 coils. The reconstructions were performed in MATLAB on a PC with a 2 GHz AMD CPU.
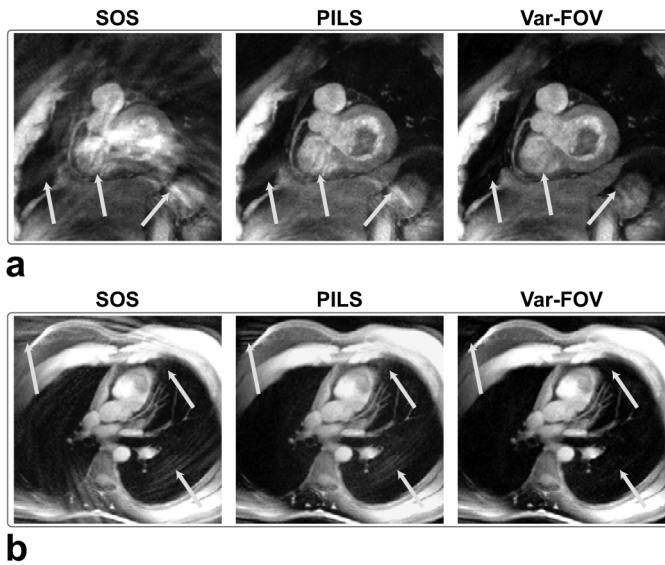

Fig. 8. Spiral coronary angiograms reconstructed with SOS, PILS, and the variable-FOV method at two different acceleration factors, $R = 1.7$ (a) and 4.5 (b). PILS reconstructions were performed with $\text{FOV}_{\text{recon}}$ supported by the highest sampling density. A moderately strong display windowing was applied to emphasize differences in the level of aliasing artifacts. In both a and b, the arrows pinpoint regions of residual artifacts in the PILS images. In contrast, the variable-FOV method reliably suppresses these artifacts. Because this method reduces noise-like aliasing from high-frequency data and uses optimal combination weights, it yields reduced noise appearance compared with PILS.

TABLE II
SNR IMPROVEMENT WITH THE VARIABLE-FOV
METHOD OVER PILS

Acceleration	% Improvement
R = 1.7	19.2±6.3 %
R = 4.5	31.1±3.9 %

For each acceleration factor, the mean percentage improvement over 5 measurement regions is listed along with the standard deviation.

PILS image using $\text{FOV}_{\text{recon}}$ supported by the lowest sampling density, due to the optimal combination weights and the extended $\text{FOV}_{\text{recon}}$ for low frequencies. Table II lists the level of improvement at each value of R, and 31.1% higher SNR was measured on average in the variable-FOV images at $R = 4.5$.

IV. DISCUSSION

In a variable-density acquisition, the denser sampling at low frequencies results in larger FOV_{acq}s compared with the periphery of k-space. The proposed technique suppresses aliasing artifacts by reconstructing undersampled high-frequency data within a smaller region, $\text{FOV}_{\text{recon-high}}$. Meanwhile, the SNR efficiency is improved by retaining the low-frequency images in a larger extent, $\text{FOV}_{\text{recon-low}}$. Finally, individual coil images are SNR-optimally combined with weights computed from data-driven sensitivity estimates.

The PILS method utilizes the same $\text{FOV}_{\text{recon}}$ for all data, and provides relatively faster and simpler reconstructions compared with the variable-FOV technique. The PILS images can be cropped to either $\text{FOV}_{\text{acq-high}}$ or $\text{FOV}_{\text{acq-low}}$ to remove aliasing artifacts or make more efficient use of the data, respectively. In contrast, the proposed method offers a favorable trade-off, and makes optimal use of the data in each k-space partition without creating artifacts. As a result, it is also more robust against suboptimally localized sensitivities.

Because both PILS and the variable-FOV method utilize coil sensitivities as anti-aliasing filters, the acceleration limits are more heavily dependent on the coil configuration than for other techniques such as SENSE or GRAPPA, particularly for uniformly undersampled trajectories. Although these techniques can offer improved artifact-suppression at higher accelerations, they also suffer from noise amplification due to the corresponding g-factors. It is important to note that regularization techniques can help improve the conditioning and the SNR of the SENSE reconstructions [39]. Nevertheless, because the proposed method does not embody a matrix inversion, it is more robust against suboptimal conditioning. For variable-FOV reconstructions, the SNR loss varies spatially depending on the portion of coils that contribute to the data reconstructed at each pixel.

While SENSE yields residual errors and artifacts in the absence of accurate sensitivity estimates, the proposed method is less sensitive to these inaccuracies. Although overweighting of low- or high-frequency data may cause localized blurring or increased noise respectively, such problems were not apparent for the reconstructions in this work. The autocalibrating SENSE and GRAPPA methods are also more tolerant to estimation errors, but the reconstructions normally incur considerable computational burden for non-Cartesian data. Contrarily, the proposed method assembles the final image with a pixel-wise linear combination following the simple gridding reconstruction and apodization steps. Therefore, the processing times are substantially reduced compared to the computationally-intensive approaches.

Potential Improvements

The proposed method has been successfully demonstrated with acceleration factors up to 4.5 for spiral trajectories, and its extensions to different trajectories and higher factors are straightforward. Nevertheless, the robustness of the technique against higher accelerations is yet to be investigated. More specialized coil designs with smaller element sizes might be essential in maintaining further accelerations.

Although the sensitivity to coil-profile errors is low, a number of approaches can help improve the estimates when necessary. The sum-of-squares normalization in the sensitivity estimates can be replaced by other factors such as weighted or nonlinear combinations [32], [40]. In addition, the obtained estimates can be further processed with polynomial fitting [6].

V. CONCLUSION

The proposed method delivers fast, noniterative, and high-SNR autocalibrating parallel image reconstructions without introducing significant artifacts. While the image SNR is improved by utilizing larger $\text{FOV}_{\text{recon}}$s for low spatial frequencies, aliasing artifacts from high frequencies are suppressed by reducing this FOV. Furthermore, the gridding reconstruction and the subsequent combination of the individual images are straightforward processes with low computational complexity. The reconstruction speed of the proposed method will particularly benefit applications based on non-Cartesian acquisitions.

APPENDIX

Derivation of the Autocorrelation Function: Assuming P denotes the image intensity at spatial location (x, y), and $\tilde{P}^*$ is the conjugate intensity at location $(\tilde{x}, \tilde{y})$, the autocorrelation function is given by (13), shown at the bottom of the page. To simplify the analysis, the low- and high-frequency component images (S_i^L and S_i^H) can be considered as zero-mean processes without loss of generality. Since S_i^L and S_i^H are reconstructed from separate sets of k-space samples, these images are uncorrelated and the corresponding cross terms are eliminated

$$R_P = \sum_{i,j} \mathrm{E}\left\{ S_i^L w_i^L (\tilde{S}_j^L \tilde{w}_j^L)^* + S_i^H w_i^H (\tilde{S}_j^H \tilde{w}_j^H)^* \right\}. \quad (14)$$

The autocorrelation can then be expressed as a weighted combination of the cross-correlation functions for the individual component images $R_{ij}^{L,H} = \mathrm{E}\left\{ S_i^{L,H} (\tilde{S}_j^{L,H})^* \right\}$

$$R_P = \sum_{i,j} \left(R_{ij}^L w_i^L (\tilde{w}_j^L)^* + R_{ij}^H w_i^H (\tilde{w}_j^H)^* \right). \quad (15)$$

In this work, we adopt a bivariate white Gaussian noise model for the acquired MR data, and only consider the noise correlation among coils that collect samples at identical k-space locations [16]. With these assumptions, the cross-correlation for the full-resolution image, $R_{ij} = \mathrm{E}\left\{ S_i (\tilde{S}_j)^* \right\}$, is equal to the corresponding entry of the noise correlation matrix, σ_{ij}^2. It is important to note that $S_i = S_i^L + S_i^H$, where S_i^L and S_i^H are band-pass filtered versions of S_i. Therefore, the cross-correlation functions R_{ij}^L and R_{ij}^H are proportional to the inverse

Fourier transforms of the corresponding magnitude-squared filter responses

$$R_{ij}^L = \sigma_{ij}^2 \, \mathrm{FT}^{-1} \left\{ |B^L|^2 \right\} \quad (16)$$

$$R_{ij}^H = \sigma_{ij}^2 \, \mathrm{FT}^{-1} \left\{ |1 - B^L|^2 \right\} \quad (17)$$

where FT^{-1} stands for the inverse Fourier transform and B^L is the Fourier domain representation of an ideal low-pass filter. Because the underlying noise process is stationary, the cross-correlation depends only on the given coil pair and the separation between the spatial coordinates (x, y) and $(\tilde{x}, \tilde{y})$.

Derivation of the Variance: The variance of image P at spatial location (x, y) can be calculated directly from (15)

$$\sigma_P^2 = \sum_{i,j} \left\{ R_{ij}^L(0,0) \, W_{ij}^L(x,y) + R_{ij}^H(0,0) \, W_{ij}^H(x,y) \right\} \quad (18)$$

where $W_{ij}^{L,H} = w_i^{L,H} (w_j^{L,H})^*$. Substituting the previously derived relations from (16) and (17) into (18)

$$\sigma_P^2 = A^L \sum_{i,j} \sigma_{ij}^2 \, W_{ij}^L(x,y) + A^H \sum_{i,j} \sigma_{ij}^2 \, W_{ij}^H(x,y). \quad (19)$$

In the above equation, $A^{L,H}$ are constants proportional to the net area under the corresponding filters $B^{L,H}$ in the frequency domain [41]

$$A^L = \mathrm{FT}^{-1} \left\{ |B^L|^2 \right\}_{(0,0)} \quad (20)$$

$$A^H = \mathrm{FT}^{-1} \left\{ |1 - B^L|^2 \right\}_{(0,0)}. \quad (21)$$

Finally, if noise decorrelation is incorporated into the reconstruction as proposed in [16], then the noise correlation matrix becomes diagonal

$$\sigma_{ij}^2 = \begin{cases} \sigma^2, & \text{for } i = j \\ 0, & \text{otherwise.} \end{cases} \quad (22)$$

This eliminates the cross-coil terms in (19). We can further observe that the squared-sums of the coil weights, $\sum_i W_{ii}^{L,H}$, are unity with straightforward algebra. With these two additional steps, the variance can be shown to equal the variance of the underlying noise process

$$\sigma_P^2 = A^L \sigma^2 \sum_i W_{ii}^L(x,y) + A^H \sigma^2 \sum_i W_{ii}^H(x,y)$$
$$= \left(A^L + A^H \right) \sigma^2 = \sigma^2 \quad (23)$$

using the fact that $|1 - B^L|^2 = 1 - |B^L|^2$ for the considered ideal low-pass filter.

$$R_P = \mathrm{E}\left\{ \sum_{i,j} \left(S_i^L w_i^L (\tilde{S}_j^L \tilde{w}_j^L)^* + S_i^L w_i^L (\tilde{S}_j^H \tilde{w}_j^H)^* + S_i^H w_i^H (\tilde{S}_j^L \tilde{w}_j^L)^* + S_i^H w_i^H (\tilde{S}_j^H \tilde{w}_j^H)^* \right) \right\} \quad (13)$$

ACKNOWLEDGMENT

REFERENCES

[1] R. M. Heidemann, O. Ozsarlak, P. M. Parizel, J. Michiels, B. Kiefer, V. Jellus, M. Muller, F. Breuer, M. Blaimer, M. A. Griswold, and P. M. Jakob, "A brief review of parallel magnetic resonance imaging," *Eur. Radiol.*, vol. 13, no. 6, pp. 2323–2337, 2003.

[2] M. Blaimer, F. Breuer, M. Mueller, R. M. Heidemann, M. A. Griswold, and P. M. Jakob, "SMASH, SENSE, PILS, GRAPPA: How to choose the optimal method," *Top Magn. Reson. Imag.*, vol. 15, no. 4, pp. 223–36, 2004.

[3] K. P. Pruessmann, "Encoding and reconstruction in parallel MRI," *NMR Biomed.*, vol. 19, no. 3, pp. 288–299, 2006.

[4] D. K. Sodickson and W. J. Manning, "Simultaneous acquisition of spatial harmonics (SMASH): Fast imaging with radiofrequency coil arrays," *Magn. Reson. Med.*, vol. 38, no. 4, pp. 591–603, 1997.

[5] M. A. Griswold, P. M. Jakob, R. M. Heidemann, M. Nittka, V. Jellus, W. Jianmin, B. Kiefer, and A. Haase, "Generalized autocalibrating partially parallel acquisition," *Magn. Reson. Med.*, vol. 47, no. 6, pp. 1202–1210, 2002.

[6] K. P. Pruessmann, M. Weiger, M. B. Scheidegger, and P. Boesiger, "SENSE: Sensitivity encoding for fast MRI," *Magn. Reson. Med.*, vol. 42, no. 5, pp. 952–962, 1999.

[7] M. A. Griswold, P. M. Jakob, M. Nittka, J. W. Goldfarb, and A. Haase, "Partially parallel imaging with localized sensitivities (PILS)," *Magn. Reson. Med.*, vol. 44, no. 6, pp. 602–609, 2000.

[8] W. E. Kyriakos, L. P. Panych, D. F. Kacher, C. F. Westin, S. M. Bao, R. V. Mulkern, and F. A. Jolesz, "Sensitivity profiles from an array of coils for encoding and reconstruction in parallel (SpaceRIP)," *Magn. Reson. Med.*, vol. 44, pp. 301–308, 2000.

[9] E. N. Yeh, C. A. McKenzie, M. A. Ohliger, and D. K. Sodickson, "Parallel magnetic resonance imaging with adaptive radius in k-space (PARS): Constrained image reconstruction using k-space locality in radiofrequency coil encoded data," *Magn. Reson. Med.*, vol. 53, no. 6, pp. 1383–1392, 2005.

[10] P. M. Jakob, M. A. Griswold, R. R. Edelman, and D. K. Sodickson, "AUTO-SMASH: A self-calibrating technique for SMASH imaging," *Magma*, vol. 7, no. 1, pp. 42–54, 1998.

[11] R. M. Heidemann, M. A. Griswold, A. Haase, and P. M. Jakob, "VD-AUTO-SMASH imaging," *Magn. Reson. Med.*, vol. 45, no. 6, pp. 1066–1074, 2001.

[12] J. Wang, T. Kluge, M. Nittka, V. Jellus, B. Kuehn, and B. Kiefer, "Parallel acquisition techniques with modified SENSE reconstruction (mSENSE)," in *Proc. 1st Würzburg Workshop Parallel Imag.*, Würzburg, Germany, 2001, p. 92.

[13] C. A. McKenzie, E. N. Yeh, M. A. Ohliger, M. D. Price, and D. K. Sodickson, "Self-calibrating parallel imaging with automatic coil sensitivity extraction," *Magn. Reson. Med.*, vol. 47, no. 3, pp. 529–538, 2002.

[14] K. Heberlein and X. Hu, "Auto-calibrated parallel spiral imaging," *Magn. Reson. Med.*, vol. 55, no. 3, pp. 619–625, 2006.

[15] C. M. Tsai and D. G. Nishimura, "Reduced aliasing artifacts using variable-density k-space sampling trajectories," *Magn. Reson. Med.*, vol. 43, no. 3, pp. 452–458, 2000.

[16] K. P. Pruessmann, M. Weiger, P. Bornert, and P. Boesiger, "Advances in sensitivity encoding with arbitrary k-space trajectories," *Magn. Reson. Med.*, vol. 46, pp. 638–651, 2001.

[17] P. Hu, C. M. Kramer, and C. H. Meyer, "Parallel imaging based on successive convolution operations (BOSCO)," in *Proc. 15th Annu. Meeting ISMRM*, Berlin, Germany, 2007, p. 751.

[18] A. Arunachalam, A. Samsonov, and W. F. Block, "Self-calibrated GRAPPA method for 2D and 3D radial data," *Magn. Reson. Med.*, vol. 57, no. 5, pp. 931–938, 2007.

[19] N. Sinha, S. Jana, and M. Saranathan, "A neural network approach for non-Cartesian k-space parallel imaging reconstruction," in *Proc. 15th Annu. Meeting ISMRM*, Berlin, Germany, 2007, p. 336.

[20] Y. Qian, Z. Zhang, Y. Wang, and F. E. Boada, "Decomposed direct matrix inversion for fast non-Cartesian SENSE reconstructions," *Magn. Reson. Med.*, vol. 56, no. 2, pp. 356–363, 2006.

[21] K. A. Heberlein, Y. Kadah, and X. Hu, "Segmented spiral parallel imaging using GRAPPA," in *Proc. 12th Annu. Meeting ISMRM*, Kyoto, Japan, 2004, p. 328.

[22] R. M. Heidemann, M. A. Griswold, N. Seiberlich, G. Kruger, S. A. Kannengiesser, B. Kiefer, G. Wiggins, L. L. Wald, and P. M. Jakob, "Direct parallel image reconstructions for spiral trajectories using GRAPPA," *Magn. Reson. Med.*, vol. 56, no. 2, pp. 317–326, 2006.

[23] A. A. Samsonov, W. F. Block, A. Arunachalam, and A. S. Field, "Advances in locally constrained k-space-based parallel MRI," *Magn. Reson. Med.*, vol. 55, no. 2, pp. 431–438, 2006.

[24] R. M. Heidemann, M. A. Griswold, N. Seiberlich, M. Nittka, S. A. R. Kannengiesser, B. Kiefer, and P. M. Jakob, "Fast method for 1D non-Cartesian parallel imaging using GRAPPA," *Magn. Reson. Med.*, vol. 57, no. 6, pp. 1037–1046, 2007.

[25] N. Seiberlich, F. Breuer, R. Heidemann, M. Blaimer, M. Griswold, and P. Jakob, "Reconstruction of undersampled non-Cartesian data sets using pseudo-Cartesian GRAPPA in conjunction with GROG," *Magn. Reson. Med.*, vol. 59, no. 5, pp. 1127–1137, 2008.

[26] J. H. Lee, G. C. Scott, J. M. Pauly, and D. G. Nishimura, "Broadband multicoil imaging using multiple demodulation hardware: A feasibility study," *Magn. Reson. Med.*, vol. 54, no. 3, pp. 669–676, 2005.

[27] J. M. Santos, B. S. Hu, J. H. Lee, and J. M. Pauly, "Single breath-hold whole-heart MRA using variable density spirals and localized coil demodulation," in *Proc. 14th Annu. Meeting ISMRM*, Seattle, WA, 2006, p. 2449.

[28] B. Kressler, P. Spincemaille, T. D. Nguyen, L. Cheng, Z. X. Hai, M. R. Prince, and Y. Wang, "Three-dimensional cine imaging using variable-density spiral trajectories and SSFP with application to coronary artery angiography," *Magn. Reson. Med.*, vol. 58, no. 3, pp. 535–543, 2007.

[29] T. Çukur, J. M. Santos, D. G. Nishimura, and J. M. Pauly, "Varying kernel-extent gridding reconstruction for undersampled variable-density spirals," *Magn. Reson. Med.*, vol. 59, no. 1, pp. 196–201, 2008.

[30] M. A. Ohliger, P. Ledden, C. A. McKenzie, and D. K. Sodickson, "Effects of inductive coupling on parallel MR image reconstructions," *Magn. Reson. Med.*, vol. 52, no. 3, pp. 628–639, 2004.

[31] O. Dietrich, J. G. Raya, S. B. Reeder, M. Ingrisch, M. F. Reiser, and S. O. Schoenberg, "Influence of multichannel combination, parallel imaging and other reconstruction techniques on MRI noise characteristics," *Magn. Reson. Imag.*, vol. 26, no. 6, pp. 754–762, 2008.

[32] M. Bydder, D. J. Larkman, and J. V. Hajnal, "Combination of signals from array coils using image-based estimation of coil sensitivity profiles," *Magn. Reson. Med.*, vol. 47, no. 3, pp. 539–548, 2002.

[33] J. M. Santos, C. H. Cunningham, M. Lustig, B. A. Hargreaves, B. S. Hu, D. G. Nishimura, and J. M. Pauly, "Single breath-hold whole-heart MRA using variable-density spirals at 3T," *Magn. Reson. Med.*, vol. 55, no. 2, pp. 371–379, 2006.

[34] J. M. Santos, G. A. Wright, and J. M. Pauly, "Flexible real-time magnetic resonance imaging framework," in *Conf. Proc. IEEE Eng. Med. Biol. Soc.*, 2004, vol. 2, pp. 1048–1051.

[35] C. Meyer, J. Pauly, A. Macovski, and D. Nishimura, "Simultaneous spatial and spectral selective excitation," *Magn. Reson. Med.*, vol. 15, no. 2, pp. 287–304, 1990.

[36] A. M. Takahashi, "Consideration for using the Voronoi areas as a k-space weighting function," in *Proc. 7th Annu. Meeting ISMRM*, Philadelphia, PA, 1999, p. 92.

[37] V. Rasche, R. Proksa, R. Sinkus, P. Bornert, and H. Eggers, "Resampling of data between arbitrary grids using convolution interpolation," *IEEE Trans. Med. Imag.*, vol. 18, no. 5, pp. 385–392, 1999.

[38] J. I. Jackson, C. H. Meyer, D. G. Nishimura, and A. Macovski, "Selection of a convolution function for Fourier inversion using gridding," *IEEE Trans. Med. Imag.*, vol. 10, no. 3, pp. 473–478, 1991.

[39] F.-H. Lin, K. K. Kwong, J. W. Belliveau, and L. L. Wald, "Parallel imaging reconstruction using automatic regularization," *Magn. Reson. Med.*, vol. 51, no. 3, pp. 559–567, 2004.

[40] T. Çukur, M. Lustig, and D. G. Nishimura, "Multiple-profile homogenous image combination: Application to phase-cycled SSFP and multicoil imaging," *Magn. Reson. Med.*, vol. 60, pp. 732–738, 2008.

[41] R. N. Bracewell, *The Fourier Transform and its Applications*, 3rd ed. New York: MGraw-Hill, 2000.